# Discrete Layer-by-Layer Magnetic Switching in Fe/MgO(001) Superlattices

R. Moubah,[1,2] F. Magnus,[1,3,*] T. Warnatz,[1] G. K. Palsson,[1] V. Kapaklis,[1] V. Ukleev,[1,4] A. Devishvili,[1] J. Palisaitis,[5] P. O. Å. Persson,[5] and B. Hjörvarsson[1]

[1]*Department of Physics and Astronomy, Uppsala University, Box 530, SE-75121 Uppsala, Sweden*
[2]*LPMMAT, Université Hassan II de Casablanca, Faculté des Sciences Ain Chock, Post box 5366 Maârif, Casablanca, Morocco*
[3]*Science Institute, University of Iceland, Dunhaga 3, IS-107 Reykjavik, Iceland*
[4]*National Research Centre "Kurchatov Institute" B. P. Konstantinov Petersburg Nuclear Physics Institute, 188300 Gatchina, Russia*
[5]*Department of Physics, Chemistry and Biology, Linköping University, SE-58183 Linköping, Sweden*
(Received 9 September 2015; revised manuscript received 27 January 2016; published 19 April 2016)

We report on a discrete layer-by-layer magnetic switching in Fe/MgO superlattices driven by an antiferromagnetic interlayer exchange coupling. The strong interlayer coupling is mediated by tunneling through MgO layers with thicknesses up to at least 1.8 nm, and the coupling strength varies with MgO thickness. Furthermore, the competition between the interlayer coupling and magnetocrystalline anisotropy stabilizes both 90° and 180° periodic alignment of adjacent layers throughout the entire superlattice. The tunable layer-by-layer switching, coupled with the giant tunneling magnetoresistance of Fe/MgO/Fe junctions, is an appealing combination for three-dimensional spintronic memories and logic devices.

DOI: 10.1103/PhysRevApplied.5.044011

## I. INTRODUCTION

The discovery of the large tunneling magnetoresistance (TMR) in MgO-based magnetic tunnel junctions (MTJs) with Fe and CoFe electrodes has sparked an intense research effort on the transport properties of such structures [1–4]. As a result, MgO TMR structures are central to many current and proposed spintronic-device concepts such as magnetic memory, sensors, and logic [5,6]. It is less well known that high-quality crystalline Fe/MgO/Fe(001) structures exhibit an interlayer exchange coupling (IEC) resulting in either a preferred ferromagnetic, antiferromagnetic, or even 90° in-plane alignment of the Fe layers, depending on the MgO thickness, temperature, and growth conditions [7–11]. Typically, interlayer exchange coupling has been observed in metallic multilayers and takes place through Ruderman-Kittel-Kasuya-Yosida interactions which result in a decaying oscillatory ferromagnetic-antiferromagnetic coupling with increasing spacer thickness [12]. In the case of Fe/MgO, the IEC is believed to be mediated by spin-polarized tunneling [7,13,14] through the MgO, and so the coupling strength decays exponentially with increasing MgO thickness without oscillating, with significant coupling previously observed only through MgO layers less than 1-nm thick. However, the precise mechanism governing the nature of the coupling is not fully understood. The presence of oxygen vacancies in the MgO layer are thought to be crucial to obtaining an antiferromagnetic coupling [8,9], and it has been suggested that magnetic impurities in the MgO can give rise to a biquadratic coupling term (with an associated 90° alignment of adjacent layers) [11].

Here, we show that an IEC can be achieved throughout an entire MgO/Fe(001) superlattice (the crystalline counterpart of a multilayer) with nine back-to-back MTJs. An antiferromagnetic coupling exists up to an MgO thickness of at least 1.8 nm, and results in a sequential discrete switching of the magnetic layers when subject to an applied magnetic field. The coupling is tunable through the MgO thickness and can result in a 180° or 90° in-plane alignment of adjacent layers due to the competition with the intrinsic magnetocrystalline anisotropy of Fe.

## II. EXPERIMENTAL METHODS

The Fe/MgO superlattices are grown by magnetron sputtering. The base pressure of the chamber is below $2 \times 10^{-9}$ mbar and the operating pressure of Ar gas (99.999 99%) is $2.7 \times 10^{-3}$ mbar. Prior to the growth, the MgO(001) substrates with a size of $(10 \times 10 \times 0.5)\,\mathrm{mm}^3$ are annealed at 550 °C for 1 hour. The substrate temperature during deposition is kept constant at 165 °C. The Fe layers with a constant thickness of 2.3 nm are deposited from an Fe target (of 99.95% purity) using dc sputtering, while the MgO layers are deposited using a MgO target (of 99.9% purity) with a rf source. 10–15 repetitions of Fe/MgO bilayers are grown, all starting with the growth of Fe on the MgO(001) substrates. The MgO thickness is varied, in the range 1.8 to 2.2 nm. Finally, a 1.5-nm-thick capping layer of $Al_2O_3$ is rf sputtered to protect the sample from air.

X-ray reflectivity (XRR) and diffraction (XRD) measurements are performed in order to determine the

*fridrik.magnus@physics.uu.se

 

thickness of the layers and the roughness of interfaces, using a Bruker D8 diffractometer (Cu $K_\alpha = 1.5418$ Å) equipped with a Göbel mirror on the incident side. The local crystal structure and layering are investigated by scanning transmission electron microscopy (STEM) combined with high-angle annular dark-field imaging in the double-corrected Linköping FEI Titan$^3$ 60-300, operated at 300 kV. STEM images are recorded under strong elemental contrast conditions using an optimized 30-mrad convergence semiangle which provided sub-Ångström resolution probes with 0.1-nA current. The TEM samples are prepared using a traditional "sandwich" method which includes sample cutting, mounting into the support grid, gluing, and mechanical polishing. Electron transparency of the sample is achieved by $Ar^+$ ion milling with 5-keV ion energy where the ion energy is gradually reduced to 2 keV during the final step of milling to minimize the surface damage.

Magnetization measurements are performed at room temperature using a magneto-optical–Kerr-effect setup, in a longitudinal geometry, using *p*-polarized light. A magnetic field is applied in the plane of the films and the magnetic response measured parallel to the applied field.

Polarized neutron reflectometry is carried out in the Super ADAM reflectometer at the Institut Laue–Langevin in Grenoble, France [15]. The wavelength is 5.183 Å and polarization and analyzer efficiencies are 99.8% and 99.3% on the incident and receiving ends, respectively. A guide field of 1.5 mT is used to maintain the neutron polarization which is in all cases parallel to the plane of the films. This resulted in a flipping ratio ranging between 200 and 600, depending on the slit settings used. Thus, spin leakage is negligible and is not included in the data-reduction process. The data-reduction package SARED is used for data analysis. The data are put on an absolute reflectivity scale by normalizing to the direct beam at the same slit and polarization settings and divided by a monitor to account for fluctuations in the neutron flux and to correct for points measured for different lengths of time. A constant slit opening for the entire data set is chosen such that the sample is constantly overilluminated and included as a fitting parameter in the fitting procedure. Since SuperADAM is equipped with a position-sensitive detector, the background is measured simultaneously and is evaluated based on defining regions of interest on either side of the specular beam and taking the average value. Finally, the data are fitted using the GenX fitting program [16].

## III. RESULTS AND DISCUSSION

The structural quality of the samples is illustrated in Fig. 1, including both STEM and XRD and XRR data. A low-magnification cross-sectional STEM image of a complete stack with ten repetitions of Fe/MgO bilayers is shown in Fig. 1(a). As seen in the figure, all layers are continuous, with a uniform thickness (despite some waviness on the few-nanometer length scale), and the interfaces are sharp. The epitaxial quality of the sample is evident in the atomic-resolution STEM image [Fig. 1(b)]. The Fe(001) and MgO(001) lattices are in registry with each other, exhibiting an epitaxial growth of the layers throughout the entire stack thickness.

The XRR and XRD results confirm that the structural perfection demonstrated locally by STEM is representative of the entire sample. The measured XRR of a $[\mathrm{Fe}(27\ \text{Å})/\mathrm{MgO}(18\ \text{Å})] \times 15$ superlattice is shown in Fig. 1(c). Clear total-thickness fringes can be observed, as well as multilayer Bragg peaks up to $2\theta = 14°$, as expected from the well-defined layering of the samples. In order to fit the data, we allow the thickness of each layer to vary independently by $\pm 1$ Å, thus accounting for atomic

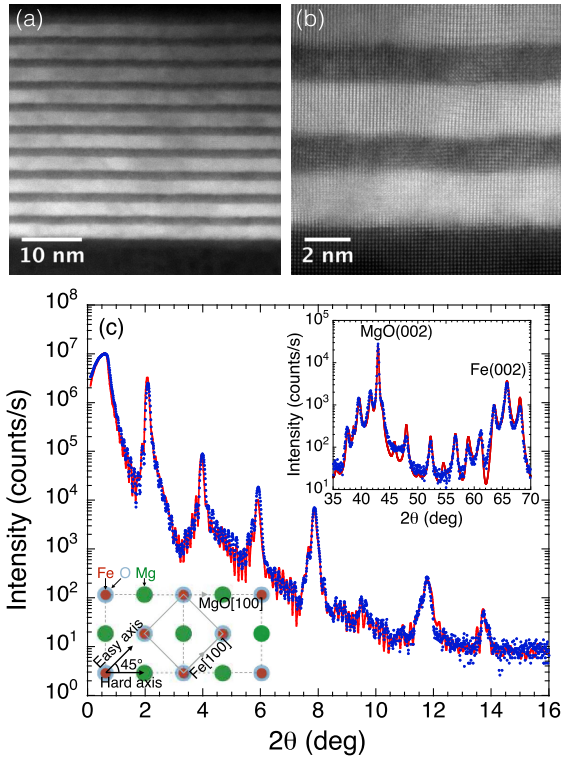


FIG. 1. Structural properties of the superlattice. (a) Cross-sectional STEM image of a sample with 10 repetitions of Fe/MgO bilayers. (b) Atomic-resolution image showing the well-defined ordering of the Fe(001) and MgO(001) lattice. (c) Experimental x-ray reflectivity scan (blue points) of a complete stack of $\mathrm{MgO}(001)/[\mathrm{Fe}(27\ \text{Å})/\mathrm{MgO}(18\ \text{Å})] \times 15/\mathrm{Al_2O_3}(18\ \text{Å})$ demonstrating that the interfaces are sharp and the layers well defined. A fit of the reflectivity is also shown (red line). Top right inset: high-angle x-ray diffraction from the same sample (blue points), showing the MgO(002) and Fe(002) peaks, as well as several superlattice peaks. The red line is a fit of the data. Bottom left inset: A schematic showing a top-view projection of the epitaxial relationship between the Fe and MgO layers. The lattice match is achieved through a 45° in-plane rotation of the Fe[100] with respect to the MgO[100].

steps in the layer thicknesses. The resulting mean thickness values are the ones given above and the Fe and MgO layer roughness is found to be 1–2 Å.

X-ray diffraction results obtained on the same sample are presented in the top-right inset of the figure. Two main peaks located at 43° and 66° are observed, corresponding to MgO(002) and Fe(002), respectively. Superlattice peaks are observed around the (002) diffraction peak of Fe and MgO, revealing a coherency of the layers. We apply the simplest disorder model possible to get a handle on the structural quality of the superlattice [17]. The model involves $N$ layers of Fe on average and $M$ layers of MgO on average repeated 15 times. Similarly to the XRR modeling described above, we allow the number of planes in each period of the superlattice to fluctuate around $N$, drawn from a Gaussian distribution with a standard deviation of $\sigma_{\mathrm{Fe}}$ and $\sigma_{\mathrm{MgO}}$. In addition, we allow a variation in the interface interatomic distance (the Fe-Mg and Fe-O distance). We include effects of absorption, the Lorentz factor, the polarization factor, atomic scattering factors, and atomic vibrations by assuming the bulk values for each material and appropriate averages. This results in an Fe thickness of 25.6 Å and a MgO thickness of 19.9 Å where the standard deviations are $\sigma_{\mathrm{Fe}} = 0.8$ Å and $\sigma_{\mathrm{MgO}} = 1.1$ Å. The out-of-plane lattice parameter of Fe is found to be expanded by 1.7%, whereas the MgO is contracted by 6%. The epitaxial relationship between Fe(001) and MgO(001) is obtained upon a 45° in-plane rotation of the Fe with respect to the MgO, as shown in the bottom-left inset of Fig. 1, and is due to the difference between the lattice parameters of Fe and MgO, which are 2.86 and 4.21 Å, respectively. Therefore, the atomic steps which form during growth with the associated thickness variations are responsible for the broadening of the Bragg-superlattice peaks in both reflectivity and diffraction.

Representative magnetization measurements obtained from an $[\mathrm{Fe}(23\ \text{Å})/\mathrm{MgO}(22\ \text{Å})] \times 10$ superlattice are displayed in Fig. 2. The discrete nature of the magnetization switching is immediately apparent from the easy-axis hysteresis loops presented in Fig. 2(a). The magnetization reversal takes place in at least 11 abrupt steps (in a sample with 10 Fe layers), indicating mixed 90° and 180° flipping of Fe layers. The regular stepwise switching, starting well before the field is reversed, is a signature of individual layers switching at different fields driven by an antiferromagnetic interlayer coupling through the MgO spacer, as we will show below. The stability of both 90° and 180° magnetic-layer configurations is a result of the large fourfold symmetric magnetocrystalline anisotropy of the Fe. The magnetocrystalline anisotropy is clear from the magnetization loop along the in-plane hard axis shown in Fig. 2(b). The in-plane hard axis is at 45° to the easy axis as shown schematically in Fig. 1. A hard-axis response is seen, typical for single-crystal Fe, with a remanence of $M_s/\sqrt{2}$, where $M_s$ is the saturation magnetization, and

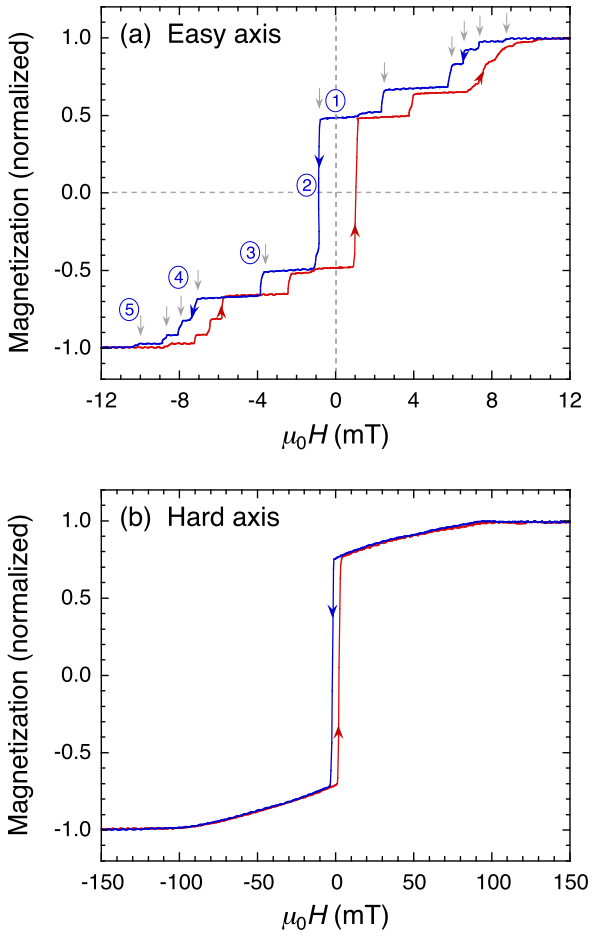


FIG. 2. Discrete magnetization switching. Room-temperature in-plane magnetization curves of an Fe(23 Å)/MgO(22 Å) superlattice with 10 repetitions. The magnetic field is applied (a) parallel to the Fe in-plane easy axis (the Fe[100] direction), and (b) parallel to the Fe in-plane hard axis (the Fe[110] direction). The colored arrows show the direction of the field sweep; the red and blue colors represent the magnetization curves when the magnetic field is swept up and down, respectively. The numbers in circles label different parts of the magnetization curve, as discussed in the text, and each symmetric step is indicated with a gray arrow.

an almost linear approach to a large saturation field $H_s$ (∼100 mT). The saturation field along the hard axis is an order of magnitude larger than along the easy axis, which is an indication of the relative sizes of the magnetocrystalline anisotropy and interlayer coupling. As a result, the steps in the easy-axis hysteresis must be due to the nucleation and motion of 90° or 180° domain walls. Crucially, we note that in samples of lesser structural quality, where the interface roughness is large or the crystal coherence is poor, we do not observe steps in the magnetization.

In order to determine the magnetic ordering in the layers, we have carried out polarized neutron reflectivity measurements. The sample is saturated along the in-plane hard axis and the field then removed, prior to the measurement,

so that the sample is in the hard-axis remanent state [at $H = 0$ in Fig. 2(b)]. The results are shown in Figs. 3(a) and 3(b). The non-spin-flip measurement shows a Bragg peak at a scattering vector value $Q_z = 2\pi/\Lambda$, where $\Lambda$ is the Fe/MgO bilayer thickness. This peak is due to the structural periodicity of the superlattice and is also seen in the XRR measurements [Fig. 1(c)]. Since the non-spin-flip channel is sensitive to the magnetization along the polarization of the incident neutrons [along the $y$ axis or Fe[110] as shown in Fig. 3(c)] this implies that the projection of magnetization along this axis has the same periodicity (in the direction parallel to $Q_z$) as the structure. Therefore, the $y$ component of the magnetization is the same in all the Fe layers. On the other hand, the spin-flip channel shows a peak at exactly half the $Q_z$ value corresponding to the Fe/MgO bilayer thickness. As the spin-flip channel is sensitive to the magnetization component along the $x$ axis this means that this component has a periodicity which is twice that of the structural periodicity. Therefore, the $x$ component of the magnetization is the same in every other Fe layer.

Simultaneous fitting of the data for three of the four spin channels (the non-spin-flip up-up and down-down channels as well as the spin-flip up-down channel) together with the XRR data shows that the hard-axis remanent magnetic state is composed of every other layer pointing at 45° to the $y$ axis and every other layer pointing at −45° to the $y$ axis, as depicted in Fig. 3(d). Thus, all layers are pointing along an easy axis as expected, but adjacent layers are at 90° to each other. Such a magnetic configuration can be achieved if there is an antiferromagnetic component to the coupling between the layers as well as a fourfold symmetric magnetic anisotropy of comparable size [10]. As can be inferred from the relative sizes of the saturation field in the easy and hard in-plane directions (see Fig. 2), the magnetocrystalline anisotropy is larger than the interlayer coupling in our case, and so the scissored 90° state is stabilized at remanence rather than a fully antiferromagnetic 180° alignment of adjacent layers. Biquadratic coupling due to magnetic impurities and oxidation of the Fe/MgO interface has also been suggested as a mechanism for 90° alignment [11] but since our samples are grown without oxygen gas in the chamber and at a relatively low temperature we do not expect this to play a significant role here. Magnetostatic coupling due to correlated or uncorrelated roughness can also give rise to interlayer coupling (ferromagnetic [18] or biquadratic [19]), but since the roughness in our samples is extremely small and the coupling disappears with increasing roughness we can deduce that this effect is weak in our samples.

The same 90° alignment of adjacent layers is also obtained when the measurement is performed at remanence with the neutron guide field along the easy axis (not shown). In this case, every other layer points along the applied-field direction and every other layer is perpendicular to the applied-field direction.

Having demonstrated that an antiferromagnetic coupling exists between the Fe layers and a stepwise switching of an entire 10-bilayer superlattice can be achieved, we now turn to the tunability of the magnetic interactions. With this in mind we have prepared superlattices with a range of MgO layer thicknesses from 16 to 22 Å. Hysteresis curves for three representative MgO spacer thicknesses are presented in Fig. 4(a). All three show qualitatively similar features, with magnetization steps and a reduced remanent magnetization. However, the remanent magnetization decreases sharply with decreasing thickness, as shown in Fig. 4(b), and at the same time the saturation field (defined as the field where the last magnetization step occurs) increases.

Although the switching fields along the easy axis are affected by the magnetocrystalline anisotropy and coercivity mechanisms, the saturation field must be proportional to

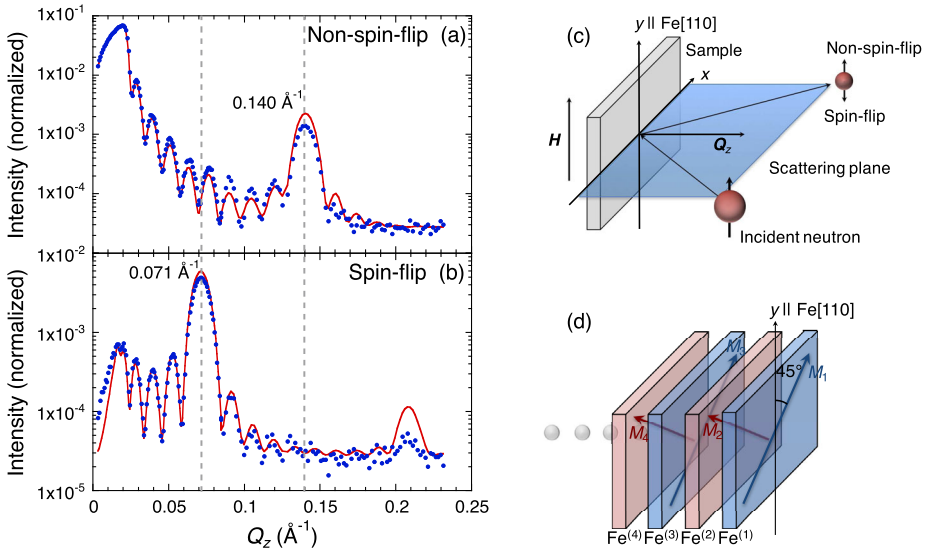


FIG. 3. Antiferromagnetic alignment of layers. Polarized neutron reflectivity measurements for the [Fe(23 Å)/MgO(22 Å)] × 10 superlattice sample in the remanent magnetic state (zero field) after saturating along the in-plane hard axis, for the non-spin-flip (a) and spin-flip (b) channels. (c) A schematic of the scattering geometry. The incident neutron has its spin aligned with the Fe[110] axis (the hard axis) and both parallel spin (non-spin-flip) and antiparallel spin (spin-flip) scattered neutrons are detected. (d) A schematic of the remanent magnetic state. The layer magnetization alternates between a −45° and +45° orientation with respect to the Fe[110] axis so that adjacent layers are at 90° to each other.

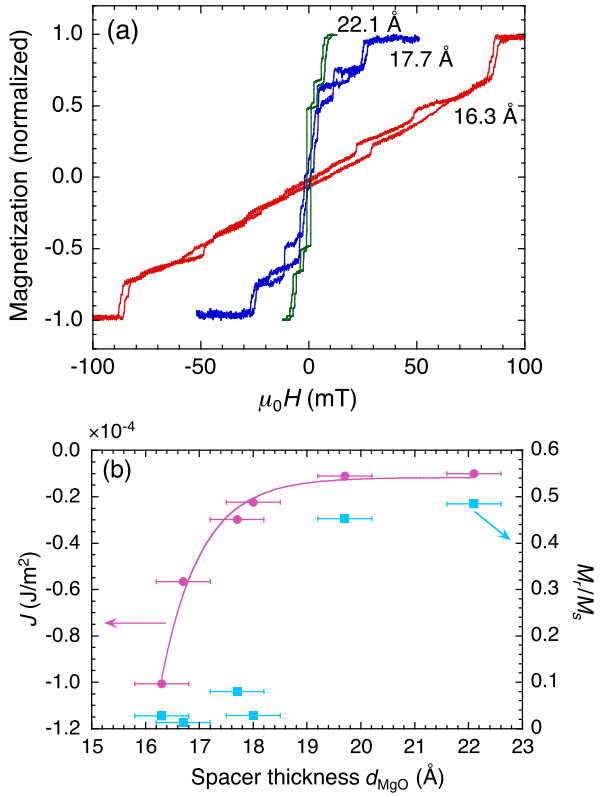


FIG. 4. Tuning the interlayer coupling. (a) Magnetization curves for three different Fe/MgO superlattices, with MgO thicknesses of 16.3, 17.7, and 22.1 Å, recorded along the Fe easy axis. (b) The MgO thickness dependence of the interlayer exchange coupling $J$ (purple circles) and the remanent magnetization $M_r$, normalized by the saturation magnetization $M_s$ (cyan squares). The solid line is a fit to the functional form $e^{-2kd_{\mathrm{MgO}}}/d_{\mathrm{MgO}}^2$.

the energy required to align the magnetization of all the Fe layers. Therefore, we can estimate the upper limit of the interlayer exchange-coupling strength from the saturation field through the relation $J = -H_s M_s d_{\mathrm{Fe}}/4$, where $d_{\mathrm{Fe}}$ is the thickness of the Fe layers [20]. This is plotted in Fig. 4(b) where by convention we denote an antiferromagnetic coupling by a negative exchange coupling. Slonczewski [13] has shown that the interlayer exchange-coupling strength across an insulating spacer layer is of the form $J \propto e^{-2kd_{\mathrm{MgO}}}/d_{\mathrm{MgO}}^2$ where $d_{\mathrm{MgO}}$ is the spacer thickness and $k = \sqrt{(U - E_F)2m_{\mathrm{eff}}/\hbar^2}$ with $U - E_F$ the tunnel barrier height, and $m_{\mathrm{eff}}$ the effective electron mass in the barrier. The variation in coupling strength should therefore dominate the saturation-field thickness dependence for small spacer thicknesses. A fit of the interlayer exchange-coupling strength $J$ to this functional form is shown in Fig. 4(b) demonstrating that our data is in good agreement with Slonczewski's model [7,13]. This further supports the presence of an antiferromagnetic interlayer exchange coupling mediated by spin-polarized tunneling through the MgO layers. However, the coupling extends through significantly thicker MgO layers than previously demonstrated [7–11].

The remanent magnetization follows a different trend. With decreasing MgO thickness ($J$ increasing in magnitude) the remanence is constant at first but then drops to almost zero. This abrupt change occurs even though the antiferromagnetic interlayer coupling is still significantly weaker than the magnetocrystalline anisotropy (as can be inferred from the size of the saturation field in the easy and hard directions, which become approximately equal only in the sample with the thinnest MgO layer). Therefore, the magnetic switching mechanism must be one of domain-wall nucleation where only a relatively small increase in the interlayer coupling strength is sufficient to tip the balance in favor of 180° alignment of adjacent layers in zero field.

With the antiferromagnetic interlayer coupling firmly established we can now explain in detail the unusual hysteresis curves shown in Fig. 2. The switching sequence is shown schematically in Fig. 5. In the easy-axis magnetization cycle [Fig. 2(a)], the remanence (labeled 1 in the figure) is $M_s/2$, which is consistent with every other layer being perpendicular to the applied field and therefore the sensitivity axis of the magnetization measurement. In a small reversed field (2) the magnetization jumps to $-M_s/2$ corresponding to a flipping of every layer by 90° so that half of the layers point in the negative direction parallel to the sensitivity axis. Since the top and bottom layer in the superlattice are affected by only half of the interlayer exchange-coupling interaction strength of the inner layers (they have only one Fe neighbor instead

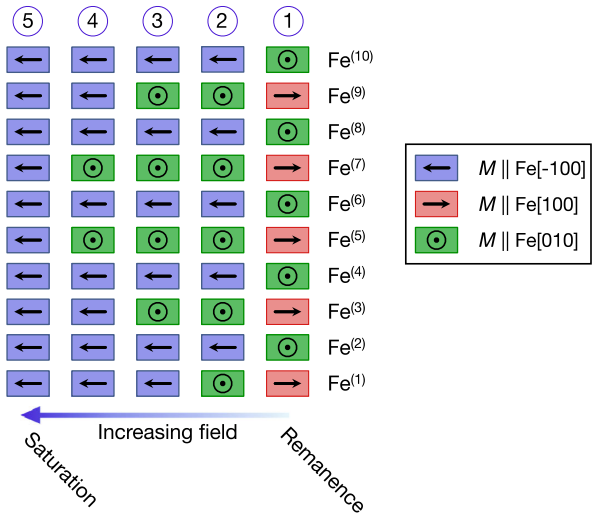


FIG. 5. Magnetic switching of the layers. A schematic of the sequence of magnetic switching, corresponding to the easy-axis hysteresis curve shown in Fig. 2. The numeric labels above the layers refer to the labels in Fig. 2. Only the Fe layers are shown, labeled $\mathrm{Fe}^{(x)}$ with $x$ denoting the number of the layer. Note that $x = 1$ could refer to either the top or bottom layer.

of two) they will be more weakly antiferromagnetically coupled than the other layers. The outermost layers will therefore switch first when the field is increased from remanence to saturation and indeed there is a step in the magnetization at 4 mT (3) or slightly below half of the saturation field. At approximately double this field, or 8 mT, a cascade of switching occurs (4), most likely from the outermost layers to the center until all layers are pointing along the applied-field direction (5). This cascade of switching is somewhat surprising since the inner layers should all switch at the same field if we assume only nearest-neighbor interlayer interactions. In the hard-axis magnetization cycle, the remanent magnetization is $M_s/\sqrt{2}$, which is consistent with all layers pointing at 45° to the applied field and the sensitivity axis. As the field is increased to saturation, the scissors close with a coherent rotation of the magnetization towards the applied-field direction, evidenced by the linear increase in magnetization up to the saturation region.

## IV. CONCLUSIONS

We have shown that stepwise layer-by-layer switching of magnetic layers can be achieved in an Fe/MgO superlattice with ten repetitions, where the Fe layers are antiferromagnetically coupled by a tunneling mechanism through the MgO layers. This antiferromagnetic coupling is highly tunable through varying the MgO thickness which, for example, could allow a magnetic shift register to be realized, as recently proposed by Lavrijsen *et al.* [21]. Furthermore, the competition between the fourfold symmetric magnetocrystalline anisotropy and the antiferromagnetic interlayer coupling could be used to stabilize more complex magnetic states with both 90° and 180° alignment of adjacent layers, opening up the possibility of new types of memory or logic devices. Since the structure is based on a series of Fe/MgO/Fe magnetic tunnel junctions, it should be possible to write in and read out the magnetic configuration highly efficiently by electrical means, thus making these structures appealing for nanoscale three-dimensional spintronic-device applications.

## ACKNOWLEDGMENTS

This work was funded by the Swedish research council (VR) and the Knut and Alice Wallenberg Foundation (KAW). In particular, KAW is acknowledged for their support of the Linköping electron microscopy laboratory.

[1] S. Yuasa, T. Nagahama, A. Fukushima, Y. Suzuki, and K. Ando, Giant room-temperature magnetoresistance in single-crystal Fe/MgO/Fe magnetic tunnel junctions, Nat. Mater. **3**, 868 (2004).

[2] S. S. P. Parkin, C. Kaiser, A. Panchula, P. M. Rice, B. Hughes, M. Samant, and S. H. Yang, Giant tunnelling magnetoresistance at room temperature with MgO (100) tunnel barriers, Nat. Mater. **3**, 862 (2004).

[3] S. Ikeda, J. Hayakawa, Y. Ashizawa, Y. M. Lee, K. Miura, H. Hasegawa, M. Tsunoda, F. Matsukura, and H. Ohno, Tunnel magnetoresistance of 604% at 300 K by suppression of Ta diffusion in CoFeB/MgO/CoFeB pseudo-spin-valves annealed at high temperature, Appl. Phys. Lett. **93**, 082508 (2008).

[4] S. Ikeda, K. Miura, H. Yamamoto, K. Mizunuma, H. D. Gan, M. Endo, S. Kanai, J. Hayakawa, F. Matsukura, and H. Ohno, A perpendicular-anisotropy CoFeB–MgO magnetic tunnel junction, Nat. Mater. **9**, 721 (2010).

[5] R. Jansen, Silicon spintronics, Nat. Mater. **11**, 400 (2012).

[6] A. Brataas, A. D. Kent, and H. Ohno, Current-induced torques in magnetic materials, Nat. Mater. **11**, 372 (2012).

[7] J. Faure-Vincent, C. Tiusan, C. Bellouard, E. Popova, M. Hehn, F. Montaigne, and A. Schuhl, Interlayer Magnetic Coupling Interactions of Two Ferromagnetic Layers by Spin Polarized Tunneling, Phys. Rev. Lett. **89**, 107206 (2002).

[8] M. Ye. Zhuravlev, E. Y. Tsymbal, and A. V. Vedyayev, Impurity-Assisted Interlayer Exchange Coupling across a Tunnel Barrier, Phys. Rev. Lett. **94**, 026806 (2005).

[9] T. Katayama, S. Yuasa, J. Velev, M. Ye. Zhuravlev, S. S. Jaswal, and E. Y. Tsymbal, Interlayer exchange coupling in Fe/MgO/Fe magnetic tunnel junctions, Appl. Phys. Lett. **89**, 112503 (2006).

[10] C. Bellouard, J. Faure-Vincent, C. Tiusan, F. Montaigne, M. Hehn, V. Leiner, H. Fritzsche, and M. Gierlings, Interlayer magnetic coupling in Fe/MgO junctions characterized by vector magnetization measurements combined with polarized neutron reflectometry, Phys. Rev. B **78**, 134429 (2008).

[11] Y. F. Chiang, Jared J. I. Wong, X. Tan, Yan Li, K. Pi, W. H. Wang, H. W. K. Tom, and R. K. Kawakami, Oxidation-induced biquadratic coupling in Co/Fe/MgO/Fe(001), Phys. Rev. B **79**, 184410 (2009).

[12] S. S. P. Parkin, N. More, and K. P. Roche, Oscillations in Exchange Coupling and Magnetoresistance in Metallic Superlattice Structures: Co/Ru, Co/Cr, and Fe/Cr, Phys. Rev. Lett. **64**, 2304 (1990).

[13] J. C. Slonczewski, Conductance and exchange coupling of two ferromagnets separated by a tunneling barrier, Phys. Rev. B **39**, 6995 (1989).

[14] P. Bruno, Theory of interlayer magnetic coupling, Phys. Rev. B **52**, 411 (1995).

[15] A. Vorobiev, A. Devishvilli, G. Pálsson, H. Rundlöf, N. Johansson, A. Olsson, A. Dennison, M. Wollf, B. Giroud, O. Aguettaz, and B. Hjörvarsson, Recent upgrade of the polarized neutron reflectometer Super ADAM, Neutron News **26**, 25 (2015).

[16] M. Björck and G. Andersson, GenX: An extensible x-ray reflectivity refinement program utilizing differential evolution, J. Appl. Crystallogr. **40**, 1174 (2007).

[17] E. E. Fullerton, I. K. Schuller, H. Vanderstraeten, and Y. Bruynseraede, Structural refinement of superlattices from x-ray diffraction, Phys. Rev. B **45**, 9292 (1992).

[18] L. Néel, C.R. Hebd. Seances Acad. Sci. **255**, 1676 (1962).

[19] S. Demokritov, E. Tsymbal, P. Grunberg, W. Zinn, and I. K. Schuller, Magnetic-dipole mechanism for biquadratic interlayer coupling, Phys. Rev. B **49**, 720 (1994).

[20] P. Poulopoulos, P. Isberg, W. Platow, W. Wisny, M. Farle, B. Hjörvarsson, and K. Baberschke, Magnetic anisotropy and exchange coupling in $Fe_nV_m$ (0 0 1) superlattices on MgO(0 0 1), J. Magn. Magn. Mater. **170**, 57 (1997).

[21] R. Lavrijsen, Ji-Hyun Lee, A. Fernández-Pacheco, D. C. M. C. Petit, R. Mansell, and R. P. Cowburn, Magnetic ratchet for three-dimensional spintronic memory and logic, Nature (London) **493**, 647 (2013).